Engineering Fracture Mechanics 271 (2022) 108632

Contents lists available at ScienceDirect

Engineering Fracture Mechanics

journal homepage: www.elsevier.com/locate/engfracmech

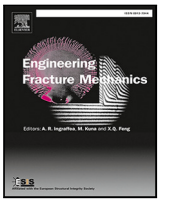

A coupled mix-mode cohesive law based on a cylindrical potential function

R. Erives [a,*], B.F. Sørensen [a], S. Goutianos [b]

[a] Technical University of Denmark, Department of Wind Energy, Risø Campus, Building 101, Frederiksborgvej 399, DK-4000 Roskilde, Denmark
[b] Norwegian University of Science and Technology, Department of Manufacturing and Civil Engineering, 2815 Gjøvik, Norway

ARTICLE INFO

Keywords:
Mix-mode cohesive laws
Cylindrical fracture resistance
Large-scale bridging
Potential based cohesive law

ABSTRACT

A novel mixed-mode cohesive law derived from a potential function is presented. The potential function is formulated using physical parameters that can be extracted from any fracture mechanics test capable of providing R-curves in terms of the J-integral as a function of the normal and tangential end-openings. The proposed cohesive law is able to describe the fracture behaviour of composites with large fracture process zones, including fibre bridging. As such, it is capable of describing both the crack tip, as well as the bridging region. An important aspect of the formulation is that the shape of the mixed-mode cohesive laws are derived and not assumed. The mixed-mode cohesive law was tested using synthetic data emulating mixed-mode fracture mechanics tests. The cohesive tractions extracted from the method exhibited characteristics which were not seeded on the model such as negative normal tractions under pure mode shear loading and non-zero shear loading under pure normal mode loading.

1. Introduction

Cohesive zone modelling is widely used in modelling of fracture problems ranging from micro-scale [1] to structural scale [2–4]. In cohesive zone modelling, the entire fracture process zone (FPZ) is described by a traction–separation law [5], also known as cohesive law. A cohesive law includes both the strength (peak traction value) and fracture energy (the combined work of the cohesive tractions). Thus, one of the main advantages of cohesive zone modelling is that both crack initiation and crack growth can be simulated [6]. This has led to the development of a large number of, mainly idealised, cohesive laws where the traction–separation laws are formulated as simple functions e.g. linear (and bi-linear) softening [7,8], trapezoidal [9,10] and exponential [11,12] functions.

A common feature of idealised cohesive laws is that the shape of the normal and shear tractions are coupled in a specific, predefined manner, or uncoupled from each other so that the normal traction, σ_n, depends only on the normal opening, δ_n, and the shear traction, σ_t, depends on the tangential opening displacement δ_t. However, in its most general form, fracture develops as mixed-mode (i.e. a combination of normal and tangential openings). In order to model mix-mode fracture, uncoupled cohesive laws can become "weakly coupled" by implementing a mix-mode failure criterion [3,13], or interaction criterion for onset and failure [14–16]. Such an approach implies that pure modes are fully-decoupled, but mixed-modes are not. Previous experimental studies suggest that mixed-mode cohesive laws are coupled, i.e. both normal and shear traction depend on each other [17,18]. Without knowledge of the physics of specific fracture to be modelled, it is difficult to prescribe a priori coupled mixed-mode cohesive laws. An alternative approach to the use of idealised cohesive laws is to derive the cohesive tractions from a coupled potential function [1,8,9,11,12,19].

* Corresponding author.
E-mail address: riea@dtu.dk (R. Erives).

https://doi.org/10.1016/j.engfracmech.2022.108632
Received 21 December 2021; Received in revised form 14 June 2022; Accepted 16 June 2022
Available online 22 June 2022

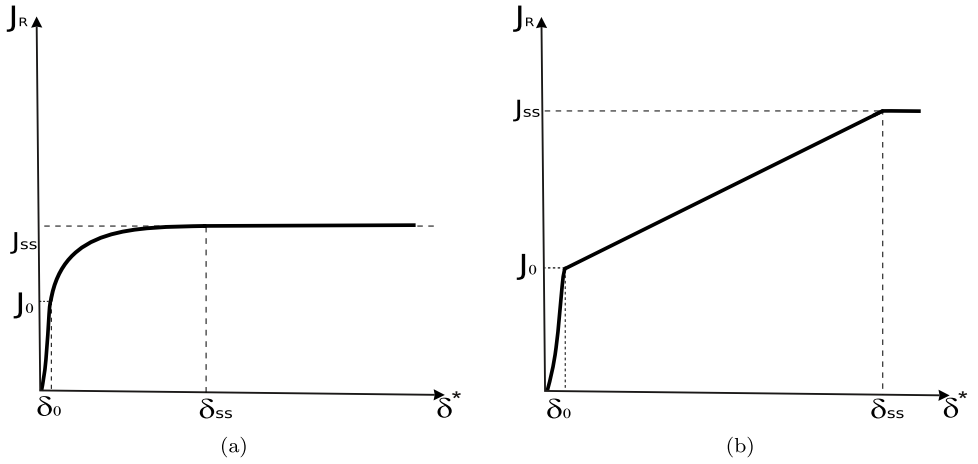

Fig. 1. Schematic of characteristic R-curve behaviour (fracture resistance as a function of magnitude of end-opening) of a crack with large scale bridging for pure (a) Mode I, (b) Mode II.

In the literature, this type of cohesive laws are commonly referred to as potential-based cohesive laws. With such an approach, one defines the potential function and the cohesive tractions are obtained by partial differentiation.

For large-scale bridging problems, the FPZ contains both a crack-tip zone and a bridging zone. For quasi-brittle materials (such as resins) the crack-tip is often small enough to be enclosed by the K-dominated region so that it conforms to linear elastic fracture mechanics (LEFM). However, the bridging region is several orders of magnitude larger than the K-dominated region, which means that the small-scale assumption, and hence LEFM, does not apply. It follows that for large-scale bridging cracking energy is dissipated both at the crack-tip and in the bridging zone. The rate at which energy is dissipated at each of the regions is quite different. The crack-tip typically observes large tractions ($10^1 - 10^2$ MPa) at very small openings ($10^0 - 10^1$ μm), while the bridging region observes small tractions ($10^{-1} - 10^0$ MPa) at very large openings ($10^0 - 10^1$ mm). Due to the very large openings related to an active bridging regime, the combined work of the cohesive tractions in the bridging regime is comparable (or even several times larger) than that of the crack-tip. A mixed-mode cohesive law should properly embody both fracture process zone regimes. This is often not the case in the literature, where most cohesive laws describe either the work dissipated by the crack tip or by the bridging region. Most published cohesive laws do not explicitly make a distinction between the crack-tip and bridging zone for mixed-mode cracking.

When a cohesive traction is defined a priori, as is the case for idealised cohesive laws, then the traction–separation law is fully determined by the combined work of the peak tractions and a critical opening (for piece-wise bi-linear laws). Then, the shape, and thus the peak traction(s), are also predefined. Furthermore, it is often difficult (or not possible for some of the idealised laws) to recover the characteristic shape of experimental R-curves from predefined/idealised cohesive tractions. The shape of a cohesive law may not be important in small-scale fracture problems [9,20]; however, it becomes important for large-scale problems e.g. delamination of fibre composites structures [21]. In particular, the shape of the cohesive law determines the stability of a structure under crack propagation [22].

By first determining a potential function that fits the shape of experimentally measured R-curves closely, we then, ensure that the combined work of the cohesive tractions closely matches the fracture resistance of the materials. In a way, the potential function is determined empirically, and the cohesive laws are derived from the potential function. It has been shown that for cohesive laws derived from a potential function, Φ, the J-integral evaluated locally around the FPZ equals the potential function evaluated at the normal and tangential end-openings [23,24]. J-integral solutions are available for standardised test configurations such as the double cantilever beam (DCB), and mixed-mode bending (MMB) among others. Sørensen and Jacobsen [25] used the J-integral based approach [24] to determine empirically mixed-mode bridging laws from measurements of the fracture resistance as a function of normal and tangential end-openings.

Measured fracture resistance of composites, expressed in terms of the J integral as a function of end-opening has several characteristics that are not well described by idealised cohesive laws. The crack initiation which occurs for very small openings is shown in R-curves as an "initiation" value, denoted J_0. With increasing opening, the fracture resistance J_R increases as a result of fibre bridging, eventually reaching a steady-state value J_{ss} once the bridging zone is fully developed. Both J_0 and J_{ss} increase with increasing mixed-mode (increasing tangential opening displacements) and the shape of the R-curves also changes with increasing mixed-mode as schematically depicted in Fig. 1. It changes from a shape with decreasing slope for normal openings (Fig. 1(a)) to a near-constant slope for near full tangential opening displacements (Fig. 1(b)). These characteristics should be reproduced by the mixed-mode cohesive laws. A model that describes accurately such decay is lacking in the literature.

In an earlier study [25], it was proposed to determine mixed-mode cohesive laws from experimental mixed-mode fracture resistance curves using a potential function, which was expressed in terms of a sum of products of the Chebyshev polynomials. The potential function was determined as the best fit to the combined fracture resistance data of all mix-mode experiments. That approach is rather general and does not put any restrictions on the shape and coupling of mixed-mode cohesive laws. However, the

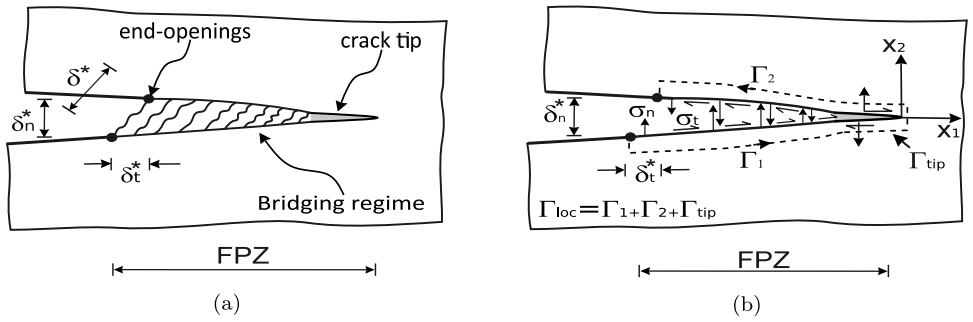

Fig. 2. Schematic of a crack under mix-mode loading and exhibiting large scale bridging (a) Definition of normal, tangential, and combined end-openings, (b) Integration paths for the evaluation of the J-integral.

method requires fracture resistance data for a wide range of mixed-modes, and limited amount of data will limit the highest degree of the Chebyshev polynomials.

The present paper proposes a novel way of getting mixed-mode cohesive laws. In comparison with the earlier method, the fit is slightly more restrictive in terms of the shape of the potential function, but it includes features that closely matches measured fracture resistance: A crack tip region with J_0 (resulting in high tractions and small openings) and a bridging zone (with small tractions and large openings) where the R-curve has a much lower slope. As such the new method is based on physical parameters. Furthermore, unlike previous similar formulations the proposed formulation covers both the crack-tip and fibre bridging regions. The potential function used in the proposed formulation is represented using cylindrical coordinates which allows to separate the potential functions into functions of the opening displacement and the phase angle. This allowed us to describe the bridging regime with a simple relationship that uses identifiable fracture parameters that characterise the R-curve behaviour for pure and mixed-modes.

Based on the above, the aim of the present study is to develop a somewhat generalised coupled mixed-mode cohesive law derived from a potential function, which avoids idealisations with respect to the cohesive law shapes and mixed-mode fracture criterion and at the same time includes both the crack tip fracture process zone and the fibre bridging zone. The parameters describing the mixed-mode cohesive law are a combination of well-defined material properties, and fitting parameters which can be extracted from standardised test configurations for which J can be calculated under large-scale bridging.

The paper is organised as follows. First, in Section 2, we develop the theory of the mixed-mode cohesive law based on cylindrical coordinates. Next in Section 3, we test the accuracy of the method using synthetic data. In Section 4, the potential function $\boldsymbol{\Phi}$, and cohesive tractions, σ_n, σ_t are presented in the $\delta_n - \delta_t$ space, as well as plots for a selected number of phase angles φ. The results are followed by a discussion in Section 5. Finally, in Section 6 the conclusions are presented.

2. Derivation of mixed-mode cohesive laws

2.1. Problem statement

Interface fracture of unidirectional composites with fibre bridging (see Fig. 2(a)) will be used as an example to build the potential function based on cylindrical coordinates, i.e. expressed in terms of the magnitude of the end-openings and their corresponding phase angle. Nonetheless, the approach is fairly general and can represent mixed-mode fracture of many interfaces. The fibres bridging at the wake of the crack lead to a large fracture process zone. Under mixed-mode fracture, the crack openings and corresponding tractions are present in both the normal and tangential directions as can be seen in Fig. 2(b). When a crack exhibits a large FPZ, linear elastic fracture mechanics (LEFM) fails to describe the fracture process. However, as explained by Suo et al. [26] problems under large FPZ can be analysed by the J-integral introduced by Rice [27]. The J-integral is defined as a path-independent contour integral, which takes the same value irrespective of which integration contour is used around a FPZ. Therefore, it can provide information about the state of the cohesive zone based on knowledge of the loads at the external boundaries.

Here, we consider a crack with a fibre bridging under mix-mode as depicted in Fig. 2(a). The J-integral evaluated along a path just outside the cohesive zone, Γ_{loc}, establishes a connection to the cohesive laws for the given interface and an evaluation of the J integral along the external boundaries connected to the applied loads. This is depicted in Fig. 2(b), where Γ_{loc} (integration path) includes both the bridging tractions and the crack-tip.

The magnitude of the normal and tangential end-openings and the phase angle between these two are defined as,

$$\delta^* = \sqrt{\delta_n^{*2} + \delta_t^{*2}}, \tag{1}$$

$$\varphi^* = tan^{-1}\left(\frac{\delta_t^*}{\delta_n^*}\right). \tag{2}$$

Note that the opening displacements at any point within the FPZ and the corresponding phase angles are denoted δ and φ (without the superscript *).

Assuming that the cohesive tractions can be derived from an energy potential

$$\boldsymbol{\Phi} = \boldsymbol{\Phi}(\delta_n, \delta_t), \tag{3}$$

$$\boldsymbol{\Phi}(0,0) = 0, \tag{4}$$

so that [28],

$$\sigma_n\left(\delta_n, \delta_t\right) = \frac{\partial \Phi\left(\delta_n, \delta_t\right)}{\partial \delta_n}, \tag{5}$$

$$\sigma_t\left(\delta_n, \delta_t\right) = \frac{\partial \Phi\left(\delta_n, \delta_t\right)}{\partial \delta_t}. \tag{6}$$

an application of the J integral around the FPZ during cracking yields [24]:

$$J_{loc} = \int_0^{\delta_n^*} \sigma_n\left(\delta_n, \delta_t\right) d\delta_n + \int_0^{\delta_t^*} \sigma_t\left(\delta_n, \delta_t\right) d\delta_t, \tag{7}$$

Inserting Eqs. (5), and (6) into Eq. (7) and carrying out the integration, gives [24],

$$J_{loc} = \Phi\left(\delta_n^*, \delta_t^*\right), \tag{8}$$

Eq. (8) implies that we can determine the potential function from measurements of the J-integral, δ_n^*, and δ_t^*. Thus, during cracking, J_{loc} equals to the fracture resistance of the material J_R. Then, the equation becomes [24]

$$J_R = J_{loc} = \boldsymbol{\Phi}(\delta_n^*, \delta_t^*), \tag{9}$$

Eq. (9) implies that the potential function Φ evaluated at the end-openings δ_n^*, and δ_t^* is identical to the J-integral. It follows that an experiment where J_R, δ_n^*, and δ_t^* increase monotonically from zero gives the potential function along the opening trace of δ_n^*, and δ_t^* [24]. Data sets from several experiments with different end-opening histories (different φ^*'s) maps $\boldsymbol{\Phi}(\delta^*, \varphi^*)$ as a function of the magnitude of the end-opening, δ^* and the phase angle φ^*. From Eq. (9) it can be observed that both the crack-tip and the bridging region are determined by the potential function $\Phi\left(\delta_n, \delta_t\right)$.

The cohesive tractions from Eqs. (5), and (6) can be visualised in a 3D Cartesian space with the normal and tangential openings on the x-y plane and the tractions perpendicular to the plane. However, for some standardised fracture tests (e.g. double cantilever beam with uneven bending moments DCB-UBM) the macroscopic normal and tangential end-openings evolve in a near proportional manner, and a cylindrical representation of the fracture resistance J_R is more natural. If the end-openings increase proportionally, then the ratio between them remains constant and so does the phase angle between them, φ^* given by (2). As such, a cylindrical representation of the fracture resistance as a function of δ^* with a fixed φ^* makes it easy to swipe through the opening plane $\delta_n^* - \delta_t^*$. This can be visualised in Fig. 3, where the straight lines represent tests at different phase angles φ^*_{1-3}, and the circles represent coordinate pairs (δ_n^*, δ_t^*) or (δ^*, φ^*). It follows that more lines, i.e. tests, would be needed for a 3D surface interpolation using Cartesian coordinates (shown Fig. 3(a)), than cylindrical coordinates (shown in Fig. 3(b)). It is therefore presumed that a cylindrical representation of the fracture resistance would yield a better surface interpolation fit.

To proceed, we apply the chain rule on Eqs. (5), and (6), and using Eq. (9) we get

$$\sigma_n(\delta, \varphi) = \cos(\varphi)\ \frac{\partial \boldsymbol{\Phi}}{\partial \delta} - \frac{\sin(\varphi)}{\delta} \frac{\partial \boldsymbol{\Phi}}{\partial \varphi}, \tag{10}$$

$$\sigma_t(\delta, \varphi) = \sin(\varphi)\ \frac{\partial \boldsymbol{\Phi}}{\partial \delta} + \frac{\cos(\varphi)}{\delta} \frac{\partial \boldsymbol{\Phi}}{\partial \varphi}, \tag{11}$$

Note, that for this formulation it is not sufficient to determine the variation in $\boldsymbol{\Phi}$ as a function of δ, the variation with respect to the phase angle φ must also be determined. It is should be noted that the above equations are valid for cases where the phase angle between normal and tangential openings remains constant. Having a constant phase angle across the small and large-scale is a simplification made for the present formulation.

2.2. Definition of fracture resistance

The cohesive tractions as derived above are based on a potential function in a cylindrical form $\boldsymbol{\Phi} = \boldsymbol{\Phi}(\delta, \varphi)$. A schematic of the 3D potential function is shown in Fig. 4(b), and a 2D schematic plot for a given phase angle φ^* is shown in Fig. 4(a). From Eq. (9) it follows that such a potential function corresponds to the combined work of the cohesive tractions. The potential function is defined as a piece-wise continuous function using two different functions in order to represent the fracture processes at both the crack tip and bridging regime. Nonetheless, the potential function is defined so that it is a continuous function from zero opening to the end-opening where a steady state fracture is attained at δ_{ss}. Continuity of the potential function is physically relevant, given that it is formulated from an energy perspective. The potential function is then

$$\Phi(\delta, \varphi) = \begin{cases} \Phi_{CT}(\delta, \varphi) & for \quad (0 < \delta \le \delta_0\ ,\ 0 \le \varphi \le 2\pi) \\ \Phi_B(\delta, \varphi) & for \quad (\delta_0 < \delta \le \delta_{ss}\ ,\ 0 \le \varphi \le 2\pi) \end{cases} \tag{12}$$

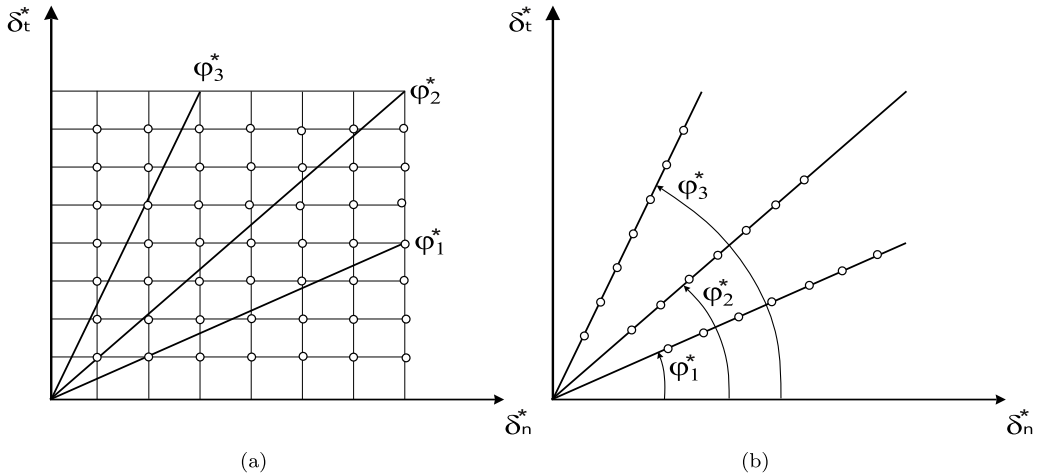

Fig. 3. Mix-mode opening plane at different end-opening phase angles (a) Cartesian coordinates (b) cylindrical coordinates.

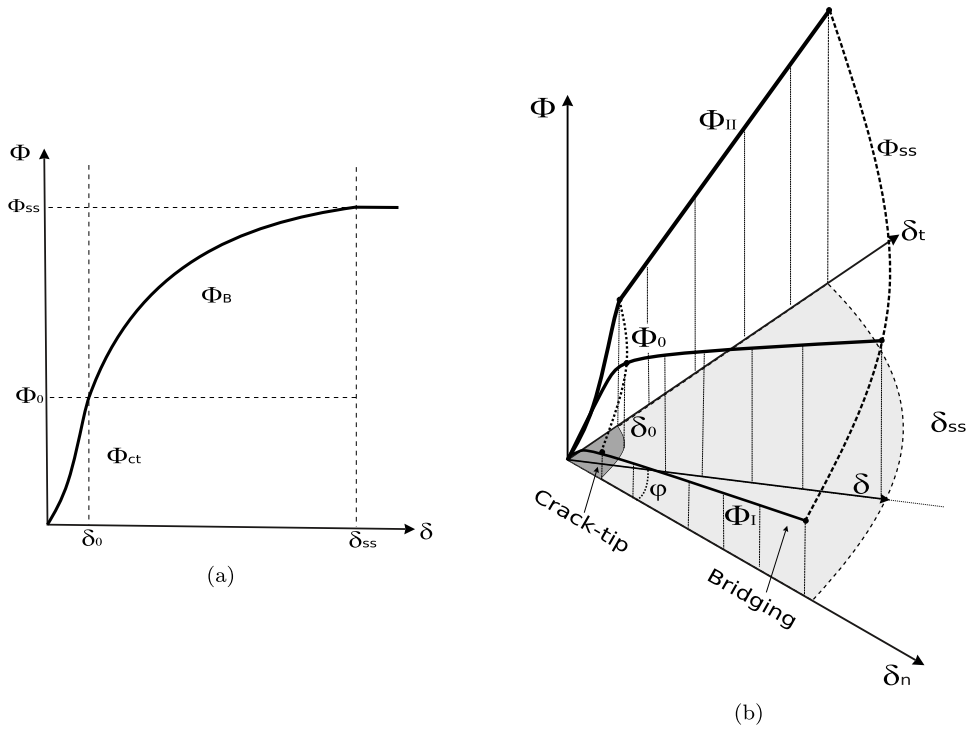

Fig. 4. Schematic of the potential function in (a) 2D for a fixed φ and (b) in 3D for any phase angle.

where subscript CT, and B indicate the crack tip and the bridging region respectively.

Based on previous experimental crack-tip fracture resistance curves [29] the fracture resistance at the crack-tip is approximated using a 3rd degree polynomial for the potential function in the crack-tip region Φ_{CT}. This also allows for smother transitions between the crack-tip and bridging traction. The potential function is

$$\Phi_{CT}(\delta,\varphi) = C_3(\varphi)\delta^3 + C_2(\varphi)\delta^2 + C_1(\varphi)\delta + C_0(\varphi), \tag{13}$$

where the variables $C_0(\varphi) - C_3(\varphi)$ are continuous and differentiable functions (for $0 < \delta \leq \delta_0$) of the phase angle φ only. The partial derivatives of Φ_{CT} with respect to the magnitude of end-openings and the phase angle are

$$\frac{\partial \Phi_{CT}}{\partial \delta} = 3C_3(\varphi)\delta^2 + 2C_2(\varphi)\delta + C_1(\varphi), \tag{14}$$

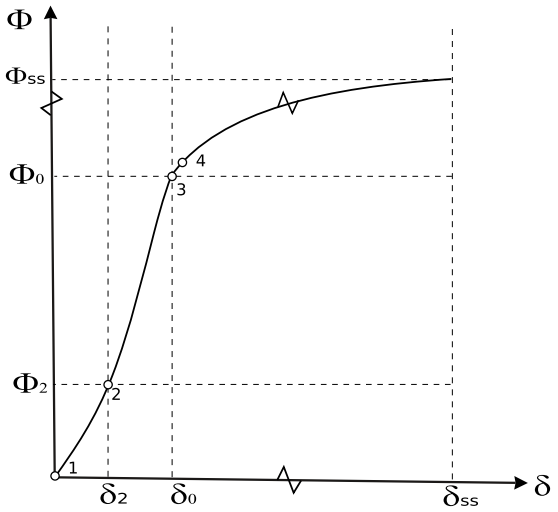

Fig. 5. Schematic of the required fracture parameters to fit the potential function as a function of the magnitude of the openings.

and,

$$\frac{\partial \boldsymbol{\Phi}_{CT}}{\partial \varphi} = \frac{\partial C_3}{\partial \varphi}\delta^3 + \frac{\partial C_2}{\partial \varphi}\delta^2 + \frac{\partial C_1}{\partial \varphi}\delta + \frac{\partial C_0}{\partial \varphi}. \tag{15}$$

The crack-tip potential function, $\boldsymbol{\Phi}_{CT}$, does not explicitly use physical parameters. Nonetheless, to determine the coefficients $C_0 - C_3$ physical parameters such as δ_{00}, J_{00}, δ_0, and J_0 are used. This is shown in Fig. 5 where the points 1–4 are defined using the physical parameters previously mentioned from an experimental R-curve. In the section below it will be explained how these points are obtained.

In the bridging region (denoted with a subscript B), a power law equation is proposed. The equation is formulated using physical parameters, such as the fracture resistance and opening at the onset of cracking, and at steady-state fracture resistance (using subscripts 0, and ss respectively), but also a shape parameter, ζ. These are obtained from experimental R-curves in terms of the end-openings and the J-integral. The proposed equation for the potential function representing the bridging zone, $\boldsymbol{\Phi}_B$, is

$$\boldsymbol{\Phi}_B(\delta, \varphi) = \boldsymbol{\Phi}_0 + \Delta\boldsymbol{\Phi}_{ss}\left(\frac{\delta - \delta_0}{\delta_{ss}}\right)^{\zeta}, \tag{16}$$

where the parameters $\boldsymbol{\Phi}_0$, $\Delta\boldsymbol{\Phi}_{ss}$, δ_0, δ_{ss}, and ζ all are functions of the phase angle φ only. After partial differentiation with respect to the end opening we get

$$\frac{\partial \boldsymbol{\Phi}_B}{\partial \delta} = \frac{\Delta\boldsymbol{\Phi}_{ss}}{\delta_{ss}}\zeta\left(\frac{\delta - \delta_0}{\delta_{ss}}\right)^{\zeta - 1}, \tag{17}$$

and after partial derivation with respect to the phase angle and some algebraic re-arrangements,

$$\frac{\partial \boldsymbol{\Phi}_B}{\partial \varphi} = \frac{\partial \boldsymbol{\Phi}_0}{\partial \varphi} + \frac{\partial(\Delta\boldsymbol{\Phi}_{ss})}{\partial \varphi}D + \Delta\boldsymbol{\Phi}_{ss}\left[A\frac{\partial \delta_0}{\partial \varphi} + B\frac{\partial \delta_{ss}}{\partial \varphi} + C\frac{\partial \zeta}{\partial \varphi}\right], \tag{18}$$

where the parameters A, B, C and D are given by

$$A = -D\xi\frac{1}{\delta - \delta_0}, \tag{19}$$

$$B = -D\frac{\zeta}{\delta_{ss}}, \tag{20}$$

$$C = \ln\left\{\frac{\delta - \delta_0}{\delta_{ss}}\right\} D, \tag{21}$$

$$D = \left(\frac{\delta - \delta_0}{\delta_{ss}}\right)^{\zeta}. \tag{22}$$

Note that both $\boldsymbol{\Phi}_{CT}$, and $\boldsymbol{\Phi}_B$ are continuous and differentiable functions. As such $\boldsymbol{\Phi}$ is also continuous, and differentiable within the ranges $0 < \delta < \delta_0$ and $\delta_0 < \delta < \delta_{ss}$, but it does not need to be differentiable at the border of $\boldsymbol{\Phi}_{CT}$, and $\boldsymbol{\Phi}_B$ (at $\delta = \delta_0$ for any φ).

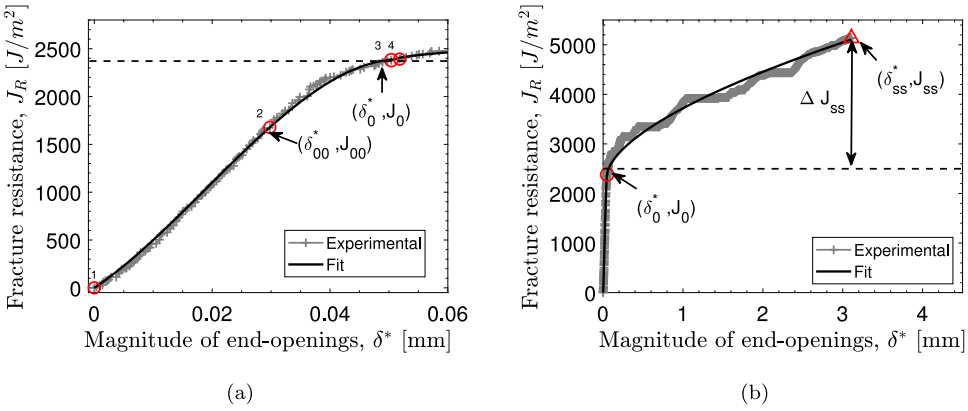

Fig. 6. Example of extraction of fracture parameters from a given set of experimental R-curve data (Step 1), J_R as a function of magnitude of end-openings. *Source:* Experimental data from [32].

3. Methods

3.1. Extraction of fracture parameters

The extraction of the parameters that describe the potential function is carried out in two steps (1) determination of fracture and fitting parameters for the individual phase angle of the end-openings, φ^*, and (2) determination of smooth functions that cover the full range ($0° \leq \varphi^* \leq 90°$) of the tested phase angles. In Step (1) the initiation, and steady-state fracture parameters are simply read from the R-curves at a given phase angle, i.e., $J_0(\varphi_1^*)$, $\delta_0(\varphi_1^*)$, $J_{ss}(\varphi_1^*)$, $\delta_{ss}(\varphi_1^*)$ (See Fig. 6). This requires some criteria to define fracture onset and steady-state. The determination of these parameters is a non-trivial process, nonetheless, it is out of the scope of the present work, and as such, it is assumed that onset and steady-state are known, well-defined points in the R-curves. It should be noted that high precision measurements (in the order of a micron) are required to characterise the fracture resistance at the crack-tip region. Experimental R-curves with the sufficient accuracy and precision have been measured in the past [29–31]. Having defined the openings at crack initiation and at steady-state, then the shape parameter, ζ, can be fitted to the experimental $J_R - \delta^*$ data (using Eq. (16)) for each φ^* (independently for each experiment). A non-linear least-squares solver can be used to fit Eq. (16) using ζ as a fitting variable. Then, in step 2, a polynomial is fitted to these parameters (the set of measurements listed above) in order to cover the entire fracture resistance data. With these parameters represented in a continuous polynomial form as a function of φ^*, then the potential function can be represented as a 3D continuous function $\boldsymbol{\Phi} = \boldsymbol{\Phi}(\delta^*, \varphi^*)$ (or $\boldsymbol{\Phi} = \boldsymbol{\Phi}(\delta_n, \delta_t)$ since δ^* has undergone all values of δ for $\varphi = \varphi^*$). The polynomial fits of the parameters produce a set of coefficients representing each of the fitted fracture parameters as shown in Table 1.

3.2. Example of application

Fig. 6, shows an example of the process of extracting the parameters given a measured R-curve, as well as the fitting variable. In Fig. 6, the grey markers represent measured values of J_R as a function of the magnitude of the end-opening, δ^*, while the solid line represents the fitted J_R (for a fixed phase value φ^*). The coordinate points required to calculate the coefficients for the polynomial fit of the crack-tip fracture resistance (Eq. (13)) are shown in Fig. 6(a), while the fracture parameters required for the fracture resistance of the bridging zone are shown in 6(b). Step 1 is repeated for each tested specimen (covering different φ^*'s), which provides a set of discrete data points for each parameter.

In order to investigate the feasibility of the method, the proposed mix-mode cohesive law is first tested using synthetic $J_R - \delta^*$ data. Such data was constructed based on the polynomials of the fracture and fitting parameters needed to define the potential function (see Eqs. (16), (13) and Figs. 4 and 5) for the entire opening range. In the present study the parameters $J_0(\varphi^*)$, $J_{ss}(\varphi^*)$, $J_{00}(\varphi^*)$, $\delta_0(\varphi^*)$, $\delta ss(\varphi^*)$, $\delta_{00}(\varphi^*)$, $\zeta(\varphi^*)$ are chosen somewhat arbitrarily but such that the obtained potential function mimics the characteristic shape of typical experimental R-curves from mixed-mode fracture mechanics test. Two different data sets, namely Data Set 1 and Data Set 2 are used in order to test the sensitivity of the formulation to different input parameters. The coefficients of the imposed parameter's polynomials of Data Set 1 and Data Set 2 are listed in Table 1.

Each set of data in Table 1 constitutes a complete set of parameter which are required for the proposed formulation. Note that these values were imposed in order to test the method; however, in the determination of mixed-mode cohesive laws these parameters should be extracted from measured R-curves as described in Section 3.1. The parameters listed in Table 1 are plotted in Fig. 7 with the solid lines representing the Data Set 1, and the dashed lines representing Data Set 2. Note that the polynomials in Figs. 7(a), and 7(b) are normalised with their maximum values corresponding to each data set.

The functions $C_0 - C_3$, which define the potential function at the crack tip region (see Eq. (13)) are obtained by fitting a 3rd-degree polynomial using 4 points (already available from Step 1) of the $J_R - \delta^*$ data at a given phase angle as shown in Fig. 5. These points

Table 1
Fracture and fitting parameter coefficients for Data Set 1 and Data Set 2.

		$f(\varphi^*) = a_n \times \varphi^{*n} + a_{n-1} \times \varphi^{*n-1} + ... + a_0$						
		$J_0(\varphi^*)$	$J_{ss}(\varphi^*)$	$\delta_0(\varphi^*)$	$\delta_{ss}(\varphi^*)$	$\delta_{00}(\varphi^*)$	$J_{00}(\varphi^*)$	$\zeta(\varphi^*)$
1	a_4	7.6E−7	0	4.7E−8	0.0	0.0	0.0	0.0
	a_3	−9.85E−5	0.0	−6.70E−6	0.0	0.0	0.0	0.0
	a_2	3.0E−3	−7.0E−4	3.0E−4	9.0E−4	0.0	0.0	0.0
	a_1	4.7E−2	1.57E−1	−1.4E−3	4.22E−2	7.9E−4	1.67E−2	6.0E−3
	a_0	2.5E−1	5.85E−1	2.17E−2	2.0E+0	3.38E−3	1.0E−1	3.75E−1
2	a_4	0.0	0.0	0.0	0.0	0.0	0.0	0.0
	a_3	6.77E−6	0.0	−1.1E−7	0.0	0.0	0.0	0.0
	a_2	−1.49E−3	−7.0E−4	−2.3E−6	9.0E−4	0.0	0.0	0.0
	a_1	1.1E−1	1.57E−1	2.6E−3	4.22E−2	7.9E−4	1.67E−2	5.6E−3
	a_0	1.03E−1	5.85E−1	1.24E−2	2.0E+0	3.38E−3	1.0E−1	5.6E−1

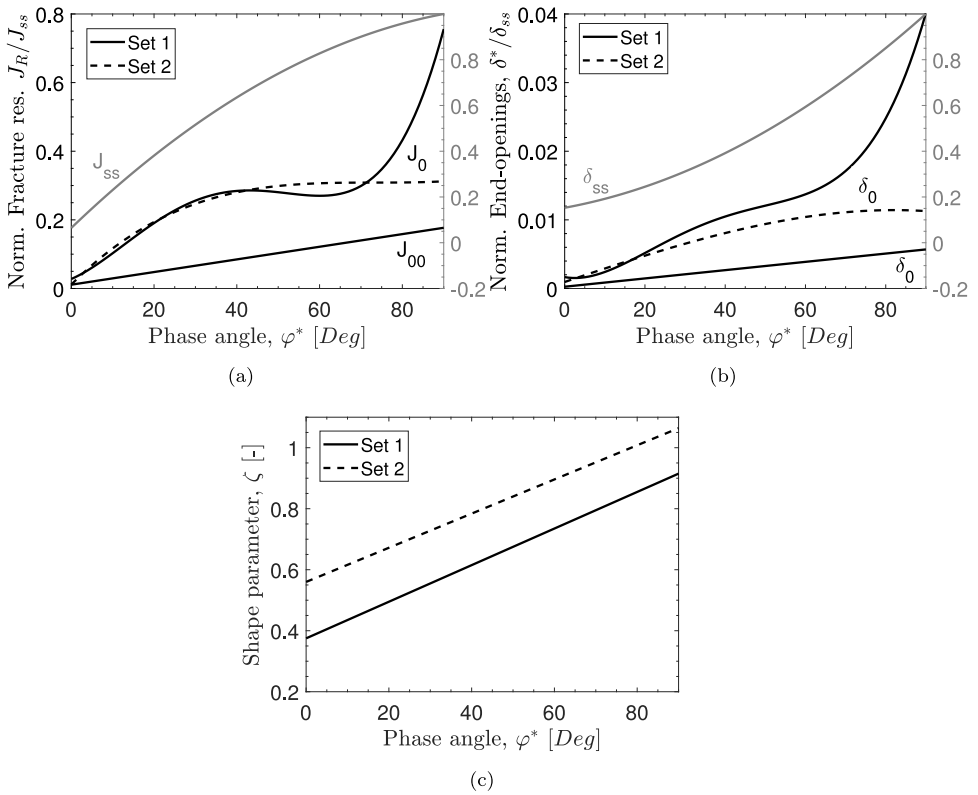

Fig. 7. Input fracture parameters from Table 1, with Data Set 1 plotted in solid lines and Data Set 2 with the dashed lines (a) Fracture resistance (b) Openings (c) Shape parameter.

are $(0,0)$, (δ_{00}, J_{00}), (δ_0, J_0), and (δ_4, J_4). The subscript "00" indicates the point at which the potential function has the largest gradient within the crack-tip zone, that is when $d\boldsymbol{\Phi} = 0$. The ordinary derivative of the potential function at the crack-tip, $\boldsymbol{\Phi}_{CT}$ is

$$dJ_R = d\boldsymbol{\Phi} = \frac{\partial \boldsymbol{\Phi}_{CT}}{\partial \delta^*} d\delta^* + \frac{\partial \boldsymbol{\Phi}}{\partial \varphi^*} d\varphi^* \tag{23}$$

and during a tests with proportional end-openings the phase angle is constant, then $d\varphi^* = 0$ so that

$$dJ_R = d\boldsymbol{\Phi} = \frac{\partial \boldsymbol{\Phi}_{CT}}{\partial \delta^*} d\delta^* \tag{24}$$

The corresponding coordinate point (opening, and corresponding fracture resistance) is then considered as the point with the largest gradient (a local maximum). The subscript 4 represents the immediate point next to (δ_0, J_0) (see Fig. 5), which is only used to try and obtain a smooth transition from the crack-tip to the bridging region.

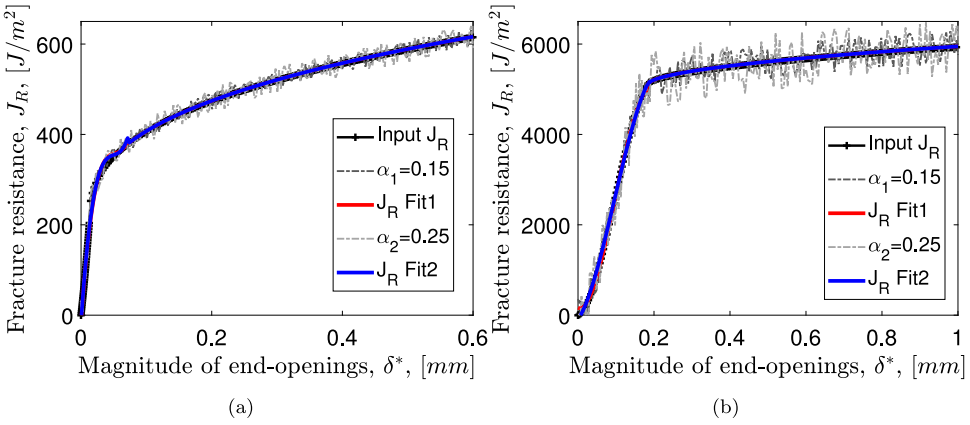

Fig. 8. Recovery of noisy fracture resistance from Data Set 1 for (a) $\varphi^* = 0°$ (b) $\varphi^* = 90°$. Note that Fit 2 curve is on top of Fit 1 so that the later is not easily observed.

4. Results

In this section the results are presented in terms of the potential function, $\Phi(\delta_n, \delta_t)$, the fracture resistance, $J_R(\delta^*, \varphi^*)$, and the cohesive tractions, $\sigma_n(\delta_n, \delta_t)$, $\sigma_t(\delta_n, \delta_t)$.

4.1. Test robustness of synthetic data

In order to test if the method is capable to handle noisy data that are common in experiments, noise was added to the generated smooth fracture resistance data, and then reconstructed by fitting (finding ζ from Eq. (16) given the noisy $J_R - \delta^*$) the noisy fracture resistance. The noise was added to the smooth $J_R(\delta^*, \varphi^*)$ data that was computed using the parameters given in Table 1. Such noise was added to each J_R value using a random number, R, (lying in the range between 0 and 1) and a scaling factor, α, as shown below

$$J_{R-n}(\delta^*) = J_R(\delta^*) + \alpha \left(R - \frac{1}{2} \right) J_0 \tag{25}$$

Two noise levels were used to generate the noisy fracture resistance J_{R-n}. This process is shown in Fig. 8 for the fracture resistance values obtained from Data Set 1. The light grey dashed line represents the largest noise level with an $\alpha_2 = 1.25$, and the dark blue line the lower noise level with an $\alpha_1 = 0.75$. This data was fitted back to reconstruct a smooth $J_R - \delta^*$ (black solid line). This procedure is shown in Fig. 8 for pure normal and tangential opening modes. The same approach is used for all individual $J_R - \delta^*$ data sets (different φ^*'s). The resulting fitted J_R values (black solid lines in Fig. 8) are almost identical to the original values (before noise) for both noise levels α_1 and α_2. Note that noise was added to the J value, but in reality, it can also be present in the data of the end-openings. This, however, was not investigated in the present study given that the proposed method requires monotonic increments of the end-openings, and such noise could be reduced during a data reduction process.

4.2. Potential function from synthetic data sets

A 3D surface plot of the fracture resistance computed using the parameters from Data Set 1 and Data Set 2 (see Table 1) are shown in Figs. 9(a) and 9(b) respectively for the entire end-opening range (δ_n^*, δ_t^*). For illustration purposes, the value of the potential function is highlighted for pure mode I and II with a solid black line, and mixed-mode values of $\varphi = 30°$ and $\varphi = 60°$ are highlighted with a dashed black line. The mixed-mode onset of fracture and steady-state values, $\Phi_0 = J_0(\varphi^*)$ and $\Phi_{ss} = J_{ss}(\varphi^*)$, are highlighted with solid red and blue lines respectively. It can be noticed that the potential function is continuous in the entire end-opening space including the transition point between the crack tip and the bridging zone. From the plots, it can be observed that the maximum value of the potential function corresponds to pure mode II, and the lowest fracture resistance occurs at pure mode I. The largest differences between the two potential functions (from Data Set 1 and Data Set 2) are located in the crack-tip region especially for large values of φ. This is somewhat expected given that the difference between the two sets are in the polynomial of the parameters δ_0, J_0.

For a better quantitative representation, curves of the potential function evaluated at $\varphi = 0°$, $\varphi = 30°$, $\varphi = 60°$, and $\varphi = 90°$ are plotted in Figs. 10(a) and 10(b) for Data Set 1 and 2 respectively. In both figures, the values corresponding to the crack tip region Φ_{CT} are shown in red, while the values at the bridging region are plotted in blue Φ_B. The steady-state fracture resistance values, beyond which the material is considered as completely failed (and the cohesive tractions are zero), is also plotted with a dashed black line. Fig. 10 shows a large variation of the potential function shape for various values of φ, and representative values such as J_0, and J_{ss} as a function of the phase angle.

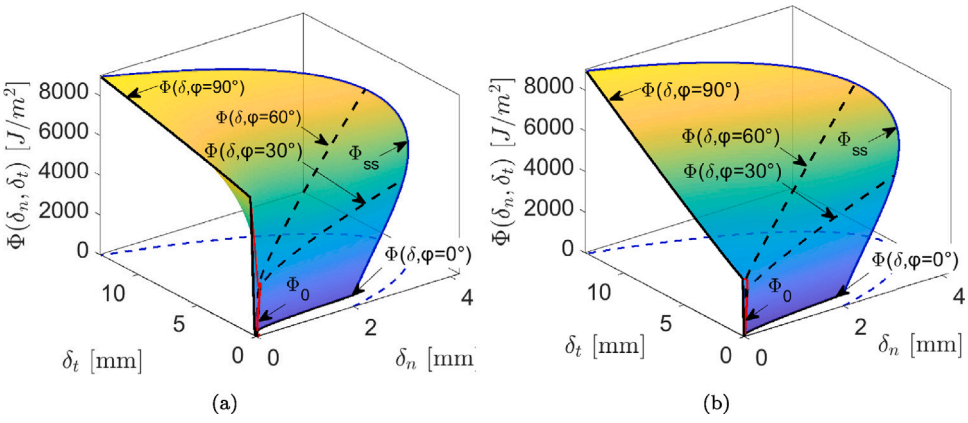

Fig. 9. Potential function $\Phi(\delta_n, \delta_t)$ for (a) Data Set 1 and (b) Data Set 2.

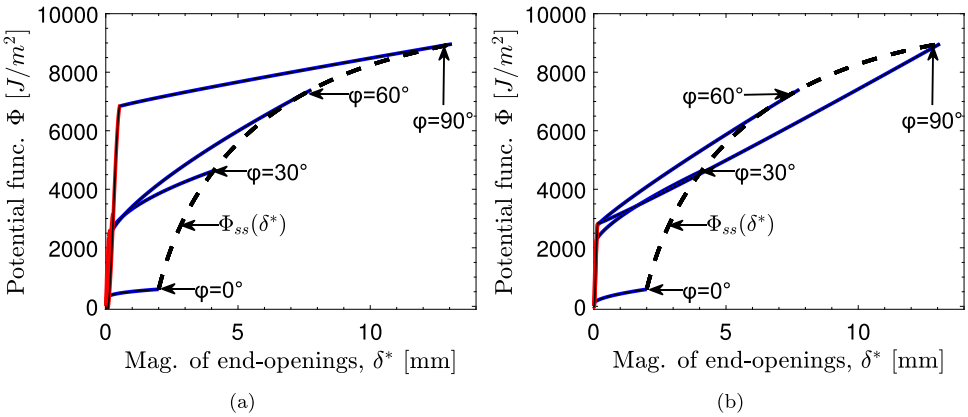

Fig. 10. Contour plots of potential function, Φ as a function of the end-opening, δ^* with the crack tip region in red, and the bridging region in blue for (a) Data Set 1 and (b) Data Set 2.

4.3. Cohesive tractions from synthetic data sets

The cohesive tractions, $\sigma_n(\delta_n, \delta_t)$, and $\sigma_t(\delta_n, \delta_t)$, computed using Data Set 1, are plotted in Figs. 11(a) and 11(b) respectively. The corresponding plots from Data Set 2 are shown in Figs. 12(a) and 12(b). These 3D plots are shown with the traction (the z-axis) cut-off in order to appreciate the shape of the bridging tractions. This is needed because the peak tractions are one order of magnitude larger than the bridging tractions (see Figs. 11 and 12). Note that both tractions σ_n and σ_t depend on both δ_n and δ_t; the derived mixed-mode cohesive laws are coupled indeed. Note also that the normal cohesive tractions from both data sets, gives negative tractions for small (near) mode II openings, and slowly reaches to a near-zero value, while σ_t sets to a near constant (non-zero) value for large δ_t; similar results have been found in other studies [25].

Contour lines of the normal and shear tractions are plotted in Fig. 13 for phase angles of $\varphi = 0°$, $\varphi = 30°$, $\varphi = 60°$, and $\varphi = 90°$ for both Data Sets. The same red/blue colouring convention to identify the crack-tip and the bridging region was used also in Fig. 10. A thin black line was placed under these curves to serve as a reference. The computed cohesive tractions have (small) discontinuities at the border between the tractions in the crack-tip and the bridging zone. As expected, each of the data sets resulted in different cohesive tractions. However, for both data sets, the maximum shear traction occurs for pure mode II (at $\varphi = 90°$), while the maximum normal traction is not corresponding to pure mode I (at $\varphi = 90°$). Also, in both instances a negative normal traction was found for pure mode II. This is further discussed in the following sections.

The peak tractions, ($\hat{\sigma}_n$, and $\hat{\sigma}_t$) and maximum bridging tractions for all φ are plotted in Figs. 14(a) and 14(b) respectively. As mentioned earlier the peak normal traction occurs at a mixed-mode phase angle of approximately $\varphi = 11°$ and $\varphi = 13°$ for Data Set 1 and 2 respectively, while the lowest peak normal traction values are found at $\varphi = 90°$ in both data sets. The maximum peak shear traction occurs at pure mode II for both data sets, while the minimum value is found at $\varphi = 0°$ for set 1 and $\varphi = 5°$ for Data Set 2. The maximum peak normal traction in the bridging region is located at $\varphi = 6°$ and $\varphi = 0°$ for Data Set 1 and 2, while the minimum value is found at $\varphi = 90°$ and $\varphi = 52°$ respectively. The peak shear tractions in the bridging region show a maximum value at $\varphi = 5°$ and $\varphi = 0°$ for Set 1 and Set 2, and a minimum value at $\varphi = 90°$ for both data sets.

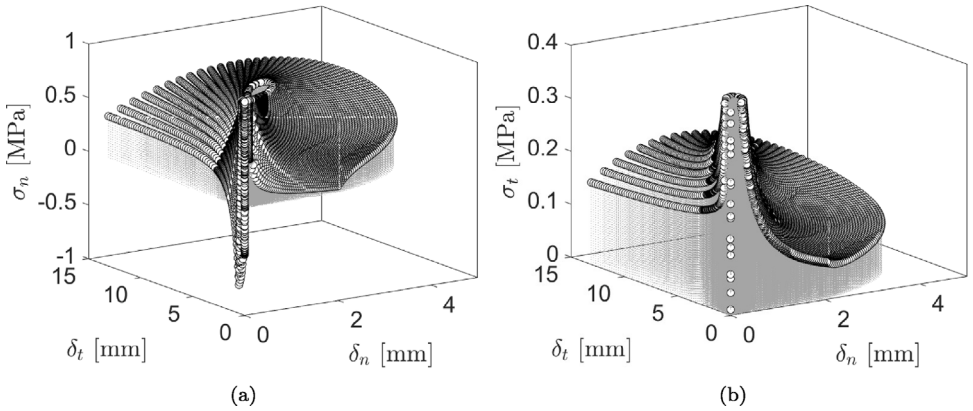

Fig. 11. Cohesive tractions from Data Set 1 where (a) σ_n is the normal traction, and (b) σ_t is the shear traction as a function of δ_n and δ_t.

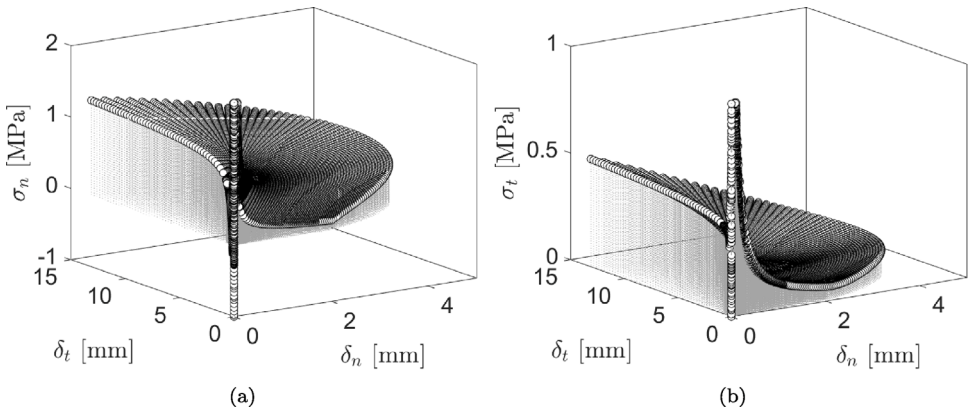

Fig. 12. Cohesive traction from Data Set 2 where (a) σ_n is the normal traction, and (b) σ_t is the shear traction as a function of δ_n and δ_t.

5. Discussion

5.1. Mathematical formulation of potential function

As mentioned in the derivation part, the proposed formulation does not require a differentiable potential function across its entire range. This might result in discontinuous cohesive tractions. The authors see no issue in having discontinuous tractions (as is the case in Fig. 13) given that discontinuities do occur in fracture (e.g. fibre snap). Nonetheless, if continuity of tractions is required for numerical reasons, then a condition can be put obtain either continuous or smother cohesive tractions in the border of $\boldsymbol{\Phi}_{CT}$, and $\boldsymbol{\Phi}_{B}$. A strict application of such a constrain on experimental data may be difficult or not possible for materials with a pronounced kink at δ_0. Scatter on the experimental data may also make it difficult to apply such a condition. Such a constraint would only be important for the numerical implementation of the cohesive law where large discontinuities in cohesive tractions should be avoided.

5.2. Restrictions on potential the potential function and cohesive laws

It is relevant to contemplate what restrictions should be imposed on the mixed-mode cohesive laws from a physics point of view. In LEFM, where the presence of the FPZ is completely ignored, linearity and symmetry arguments lead to the situation that a symmetric DCB specimen, loaded symmetric will only possess normal stresses (no shear stresses) and only normal crack opening displacement at the crack tip (Mode I). Likewise, a symmetric DCB specimen loaded asymmetric will have only shear stresses (no normal stresses) and a pure tangential crack opening displacement (Mode II) ahead of the crack tip. These symmetry arguments only hold under large-scale fracture process zone in case the interface undergoing fracture also possesses symmetry. In case the interface does not possess symmetry in the way it develops damage, there are no reason why a pure normal opening could not develop a shear traction, and likewise, there are no reason why a pure tangential opening could not induce a normal traction (M.D. Thouless, private communication [33]). For instance, a laminate made of non-crimp fabrics has backing bundles on one face only and if such fabrics are oriented with the same face up, the interface is not strictly symmetric and the decoupling into pure modes vanishes. Another example is that an interface may develop a rough fracture surface which at the micro-scale will not be symmetric;

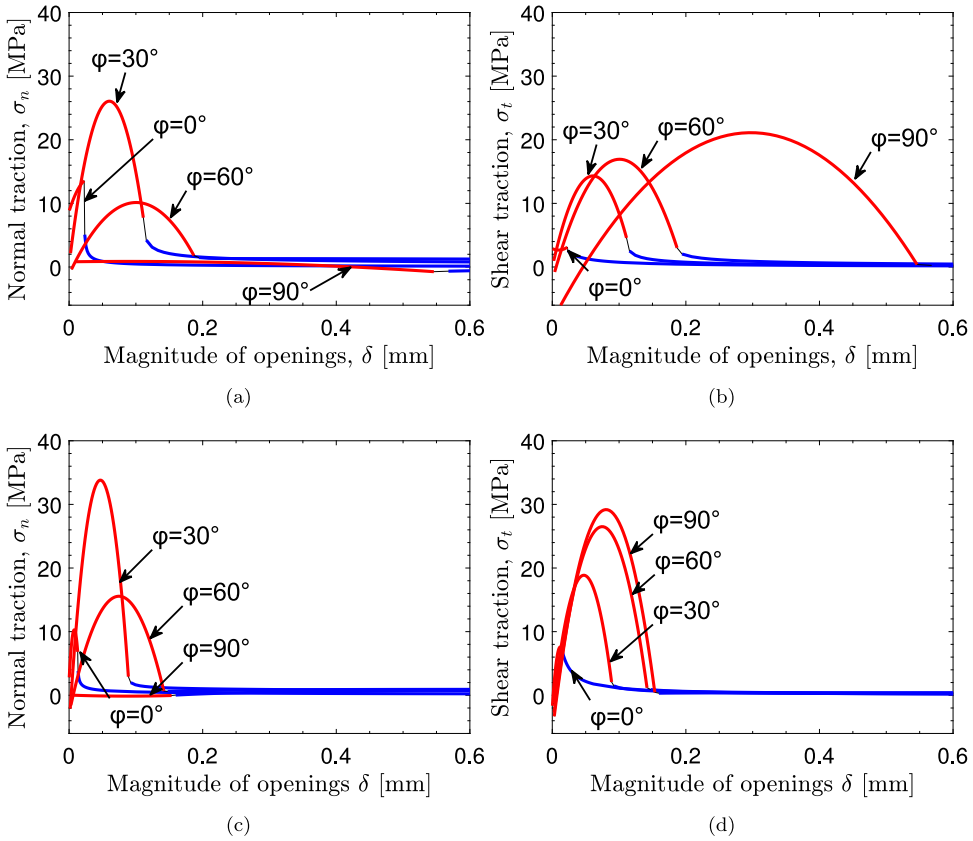

Fig. 13. Normal and shear tractions at selected phase angle values for Data Set 1 (a) and (b) and Set 2 (c) and (d)

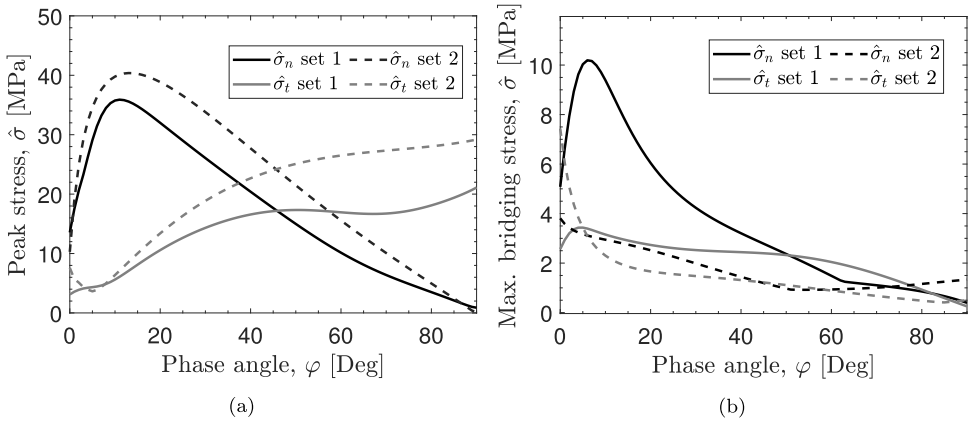

Fig. 14. Peak cohesive traction as a function of the phase angle value φ for (a) the crack-tip region and (b) the bridging regime.

conversely a pure tangential crack opening may develop a normal traction (a negative normal traction – compression – would be expected in this case [18]).

5.3. On the model assumptions

The proposed formulation is fairly general in the sense that by adapting the functional form of the potential function the same approach could potentially be used to obtain cohesive tractions of many different types of materials. However, the applicability of the method is limited to materials that do not show history dependence. Furthermore, a central assumption of the proposed method is that the φ^* remains constant in each experiment. Previous experimental studies [25] have shown that for bridge cracks, the phase

angles are indeed near constant in the bridging regime. Also, the principles of LEFM would suggest that the phase angles across the crack-tip region would also be constant. Yet, having a constant phase angle across the small and large scale is an assumption (and a limitation) of the method in its current form. It is expected that in the crack-tip regime the phase angle φ^* would conform with LEFM, but this may not be the case in the bridging region. Future work should address the form of Φ_{CT} and establish a better connection between small scale fracture (where φ^* is presumed to be identical to ψ of LEFM) and large-scale bridging, where φ^* is near-constant but different from ψ. Note that although the proposed approach analyses J_R data for a fixed φ^*, it does not assume that the phase angle of the tractions do not follow φ^*; this could lead to path-dependent mixed-mode cohesive laws [34].

Implicit in the model is the assumption of the existence of a potential function which leads to Eqs. (5) and (6). This implies that the cohesive tractions are independent of the opening-displacements history (i.e. path-independent). Path-dependent cohesive tractions have been proposed in some fracture phenomena such as plasticity and frictional sliding [35]; however, the path dependency (or lack thereof) of interface bridged fracture is to the best knowledge of the authors an unresolved problem. Path dependency is a fundamental topic that should be addressed in the future.

5.4. Model capabilities

The synthetic data from both data sets represent typical experimental data where the mode II behaviour is very different from mode I, and where there is a large variation with the phase angle, i.e. mixed-mode. Unlike other empirically determined cohesive tractions the proposed formulation is able to describe both the shape of the cohesive traction in the crack-tip, and the bridging zone. This can be seen in Fig. 13 which shows about an order of magnitude difference between the crack-tip and bridging cohesive tractions. There are a number of features of the proposed formulation which can result in a better prediction of a composite interface when loaded in a completely different configuration. For instance, determining the stability of a structure (e.g. buckling) would depend on the ability of describing accurately the shape of a cohesive traction [22]. Another examples could be the modelling of parallel cracks, where the peak stress of all interfaces needs to be known [36].

5.5. Experimental implementation

The functional form of the potential functions Φ_{CT}, and Φ_B have been proposed based on empirical observations (from the literature) of the R-curves of delamination of composite materials. Since these potential functions are fitted using experimental data, then the computed cohesive tractions (obtained from the partial differentiation of Φ) are empirically determined instead of assumed. A direct measurement of mixed-mode cohesive tractions is very complicated, however, the direct measurement of the fracture resistance using the J-integral is quite standard for large scale fracture mechanics tests (e.g. DCB-UBM). Nonetheless, experimental determination of cohesive traction by the J integral approach is challenging for small openings, i.e., at the crack tip region. First, the crack opening displacements are small, in the order of a few microns. Accurate measurement of the end-opening displacements can be made by conducting fracture experiments under optical or scanning electron microscopes where the crack opening displacements can be measured at high magnification. Second, for wide DCB specimens, the anticlastic bending makes the fracture process zone develop non-uniformly across the width [37]. This can be reduced by decreasing the beam depth (going from a plate-like geometry towards a more beam like geometry) [37].

The experimental characterisation of mixed-mode fracture commonly entails large testing campaigns. In an earlier study [25], it was concluded that a minimum of 8 different phase angles (and thus tests) are required to appropriately fit the potential function using Chebyshev polynomials. This number was given to reduce a wobbling effect which was observed in large intervals without test data. The minimum number of experiments to describe a potential function based on the proposed formulation is given by the degree of the highest polynomial for the fracture parameters in the φ^*-direction. For instance, if the largest polynomial degree is of 4th order (as is the case in Data Set 1 used in the study), then in principle a minimum of 5 tests at different phase angle values would be required to fully determine the fracture parameters that are used to calculate the potential function, i.e., J_0, J_{ss}, δ_0, δ_{ss}, and ζ as a function of φ^*. That would be a reduction in the minimum number of tests. Clearly, the polynomial forms of different materials may involve different polynomial fit, yet the use of a cylindrical form of the fracture resistance means that the potential function is fitted only to the magnitude of the end-openings as opposed to fitting it to both the normal and tangential end-openings. This is possible for DCB-UBM test where the phase angle between the normal and tangential openings come out being near constant (at least for large-scale bridging) through the test. The wobbling effect which was observed (in large intervals without test data) using Chebyshev polynomials does not appear for the proposed formulation. This is due to the fact that the approach based on the Chebyshev polynomial allows the potential function to take any shape, which gives a lot of freedom on the shape of the cohesive tractions. As a result, much more experimental data is required to compensate for it. In the proposed formulation, we "help" the fitting of the potential function by assigning a more restrictive shape (of the potential function, not of the cohesive tractions), yet, with sufficient freedom to accurately represent experimental R-curves for any mixed-mode.

6. Summary and conclusions

The derivation of a novel mix-mode cohesive law capable of capturing both the crack-tip cohesive stress, as well as the bridging stress is presented. The approach was tested using synthetic data, where the fracture and fitting parameters were represented as polynomial distributions in terms of the phase angle of the end-openings. The proposed method is fairly general and the shape of the mixed-mode cohesive laws is determined empirically as opposed to be defined a priori. The process of extracting the input

parameters from experimental R-curves is briefly described in the present work, an example is presented in Fig. 6 where it is shown that the input parameters for the potential function can be extracted from measured R-curves. Note that the fitted potential function lays practically on top of the experimental data of the fracture resistance.

Despite not making many simplifications during the derivation of the cohesive law, the obtained mixed-mode cohesive laws can be easily implemented in a finite element framework. The method is flexible and allows for different shapes of fits to the measured fracture resistance data. The method is robust against noise in the J_R data, giving almost identical fitted potential functions from two noise levels as shown in Fig. 8. After testing the proposed method, a number of conclusions can be drawn:

- The potential function can have mixed-mode dependent crack growth initiation values (J_0 and peak traction values) as well as mixed-mode dependent representation of large-scale bridging.
- The method can be implemented relatively easily as it uses only R-curves, i.e. $J_R - \delta^*$ at different phase angles of the end-openings as input. That means that in principle the method can be implemented for different mixed-mode fracture mechanics test configurations for which the normal and tangential openings evolve proportionally, and the J-integral can be calculated. Furthermore, the constitutive stiffness matrix is given in the Appendix, so its implementation as a cohesive element in FEM should be straightforward.
- The proposed potential function is capable of describing cohesive tractions both in the crack tip and bridging region. The model can represent crack tip peak traction values that are an order of magnitude larger than the tractions within the bridging zone.
- The method can be implemented using a relatively small number of mixed-mode fracture mechanics tests (different phase angles of opening). A minimum of 5 and 4 tests would be sufficient to fully describe the fracture resistance (and thus cohesive tractions) from Data Set 1 and 2 respectively.
- The constitutive stiffness matrix is given in the Appendix, so that the implementation of the cohesive law into a CZM in FEM should be straightforward.

CRediT authorship contribution statement

R. Erives: Writing – original draft, Methodology, Investigation, Funding acquisition, Formal analysis, Data curation, Conceptualization. **B.F. Sørensen:** Writing – review & editing, Supervision, Conceptualization. **S. Goutianos:** Writing – review & editing, Supervision, Methodology.

Declaration of competing interest

The authors declare that they have no known competing financial interests or personal relationships that could have appeared to influence the work reported in this paper.

Acknowledgements

The present article is part of a Ph.D. project funded partially by the Mexican National Council on Science and Technology, and the Energy Sustainability fund (CONACyT-SENER), and the RELIABLADE EUDP project supported by the Danish Energy Agency through the Energy Technology Development and Demonstration Program (EUDP), grant no. 64018-0068. The authors would like to acknowledge Albert Turon for participating in valuable discussions about the present work, as well as the anonymous reviewer for her/his insightful comments on the original manuscript.

Appendix. Cohesive stiffness matrix

The constitutive stiffness matrix K is provided for direct implementation of the cohesive law in a standard finite element code. The constitutive stiffness matrix is defined as

$$K = \begin{bmatrix} \frac{\partial \sigma_n}{\partial \delta_n} & \frac{\partial \sigma_t}{\partial \delta_n} \\ \frac{\partial \sigma_n}{\partial \delta_t} & \frac{\partial \sigma_t}{\partial \delta_t} \end{bmatrix}, \tag{26}$$

or expressed in term of the potential function

$$K = \begin{bmatrix} \frac{\partial^2 \boldsymbol{\Phi}}{\partial {\delta_n}^2} & \frac{\partial^2 \boldsymbol{\Phi}}{\partial \delta_n \partial \delta_t} \\ \frac{\partial^2 \boldsymbol{\Phi}}{\partial \delta_n \partial \delta_t} & \frac{\partial^2 \boldsymbol{\Phi}}{\partial {\delta_t}^2} \end{bmatrix}, \tag{27}$$

with

$$\frac{\partial^2 \boldsymbol{\Phi}}{\partial {\delta_n}^2} = cos^2(\varphi)\frac{\partial^2 \boldsymbol{\Phi}}{\partial \delta^2} + \frac{sin^2(\varphi)}{\delta^2}\frac{\partial^2 \boldsymbol{\Phi}}{\partial \varphi^2} - 2cos(\varphi)\frac{sin(\varphi)}{\delta}\frac{\partial^2 \boldsymbol{\Phi}}{\partial \delta \partial \varphi} + \frac{sin^2(\varphi)}{\delta}\frac{\partial \boldsymbol{\Phi}}{\partial \delta} + 2cos(\varphi)\frac{sin(\varphi)}{\delta^2}\frac{\partial \boldsymbol{\Phi}}{\partial \varphi}, \tag{28}$$

$$\frac{\partial^2 \Phi}{\partial \delta_n \partial \delta_t} = cos(\varphi)sin(\varphi)\frac{\partial^2 \Phi}{\partial \delta^2} - cos(\varphi)\frac{sin(\varphi)}{\delta^2}\frac{\partial^2 \Phi}{\partial \varphi^2} + \frac{cos^2(\varphi) - sin^2(\varphi)}{\delta}\frac{\partial^2 \Phi}{\partial \delta \partial \varphi} - \frac{cos(\varphi)sin(\varphi)}{\delta}\frac{\partial \Phi}{\partial \delta} - \frac{cos^2(\varphi) - sin^2(\varphi)}{\delta^2}\frac{\partial \Phi}{\partial \varphi}, \tag{29}$$

$$\frac{\partial^2 \Phi}{\partial {\delta_t}^2} = sin^2(\varphi)\frac{\partial^2 \Phi}{\partial \delta^2} + \frac{cos^2(\varphi)}{\delta^2}\frac{\partial^2 \Phi}{\partial \varphi^2} + 2cos(\varphi)\frac{sin(\varphi)}{\delta}\frac{\partial^2 \Phi}{\partial \delta \partial \varphi} + \frac{cos^2(\varphi)}{\delta^2}\frac{\partial \Phi}{\partial \delta} - 2cos(\varphi)\frac{sin(\varphi)}{\delta^2}\frac{\partial \Phi}{\partial \varphi}. \tag{30}$$

The partial derivatives of the proposed crack-tip potential function Φ_{CT} are

$$\frac{\partial^2 \Phi_{CT}}{\partial \delta^2} = 6C_1\delta + 2C_2, \tag{31}$$

$$\frac{\partial^2 \Phi_{CT}}{\partial \varphi^2} = \frac{\partial^2 C_3}{\partial \varphi^2}\delta^{*3} + \frac{\partial^2 C_2}{\partial \varphi^2}\delta^{*2} + \frac{\partial^2 C_1}{\partial \varphi^2}\delta + \frac{\partial^2 C_0}{\partial \varphi^2}, \tag{32}$$

and,

$$\frac{\partial^2 \Phi_{CT}}{\partial \delta \partial \varphi} = 3\frac{\partial C_1}{\partial \varphi}\delta^2 + 2\frac{\partial C_2}{\partial \varphi}\delta + \frac{\partial C_3}{\partial \varphi}. \tag{33}$$

For the bridging zone the partial derivatives of the potential function Φ_B are

$$\frac{\partial^2 \Phi_B}{\partial \delta^2} = \frac{\Delta\Phi_{ss}\zeta(\zeta - 1)}{\delta_{ss}^2}\left(\frac{\delta - \delta_0}{\delta_{ss}}\right)^{\zeta - 2}, \tag{34}$$

$$\frac{\partial^2 \Phi_B}{\partial \delta \partial \varphi} = \frac{\partial \Delta\Phi_{ss}}{\partial \varphi}\frac{\partial D}{\partial \delta} + \Delta J_{ss}\left[\frac{\partial \delta_0}{\partial \varphi}\frac{\partial A}{\partial \delta} + \frac{\partial \delta_{ss}}{\partial \varphi}\frac{\partial B}{\partial \delta} + \frac{\partial \zeta}{\partial \varphi}\frac{\partial C}{\partial \varphi}\right], \tag{35}$$

and,

$$\frac{\partial^2 \Phi_B}{\partial \varphi^2} = \frac{\partial^2 \Phi_0}{\partial \varphi^2} + \frac{\partial \Delta\Phi_{ss}}{\partial \varphi}\frac{\partial D}{\partial \delta} + \frac{\partial \Delta\Phi_{ss}}{\partial \varphi}\left[A\frac{\partial \delta_0}{\partial \varphi} + B\frac{\partial \delta_{ss}}{\partial \varphi} + C\frac{\partial \zeta}{\partial \varphi}\right] + \Delta\Phi_{ss}\left[\frac{\partial A}{\partial \varphi}\frac{\partial \delta_0}{\partial \varphi} + A\frac{\partial^2 \delta_0}{\partial \varphi^2} + \frac{\partial B}{\varphi}\frac{\partial \delta_{ss}}{\partial \varphi} + B\frac{\partial^2 \delta_{ss}}{\varphi^2} + \frac{\partial C}{\partial \varphi}\frac{\partial \zeta}{\partial \varphi} + C\frac{\partial^2 \zeta}{\partial \varphi^2}\right]. \tag{36}$$

The partial derivatives of the fracture resistance parameters $\partial\Phi_0/\partial\varphi$, $\partial\Delta\Phi_{ss}/\partial\varphi$, $\partial\delta_0/\partial\varphi$, $\partial\delta_{ss}/\partial\varphi$, $\partial\zeta/\partial\varphi$, as well as the partial derivatives of the functions $\partial C_{0-3}/\partial\varphi$, are simple polynomial derivatives and are thus not presented.

The partial derivatives of the coefficients A, B, C, and D are shown below

$$\frac{\partial A}{\partial \delta} = -D\frac{\zeta(\zeta - 1)}{(\delta_0 - \delta)^2} \tag{37}$$

$$\frac{\partial A}{\partial \varphi} = \frac{-D\zeta}{\delta - \delta_0}\left[\frac{\partial \zeta}{\partial \varphi}ln\left(\frac{\delta - \delta_0}{\delta_{ss}}\right) + \frac{\zeta\delta_{ss}}{\delta - \delta_0}\left(-\frac{1}{\delta_{ss}}\frac{\partial^* \delta_0}{\partial \varphi} - \frac{1}{\delta_{ss}^2}(\delta - \delta_0)\frac{\partial \delta_{ss}}{\partial \varphi}\right)\right] - \frac{D}{\delta - \delta_0}\frac{\partial \zeta}{\partial \varphi} - \frac{D\zeta}{(\delta - \delta_0)^2}\frac{\partial \delta_0}{\partial \varphi} \tag{38}$$

$$\frac{\partial B}{\partial \delta} = -\frac{\zeta^2}{\delta_{ss}}\frac{D}{\delta - \delta_0} \tag{39}$$

$$\frac{\partial B}{\partial \varphi} = -\frac{D\zeta}{\delta_{ss}}\left[\frac{\partial \zeta}{\partial \varphi}ln\left(\frac{\delta - \delta_0}{\delta_{ss}}\right) + \frac{\zeta\delta_{ss}}{\delta - \delta_0}\left(-\frac{1}{\delta_{ss}}\frac{\partial \delta_0}{\partial \varphi} - \frac{(\delta - \delta_0)}{\delta_{ss}^2}\frac{\partial \delta_{ss}}{\partial \varphi}\right)\right] - \frac{D}{\delta_{ss}}\frac{\partial \zeta}{\partial \varphi} + \frac{D\delta}{\delta_{ss}^2}\frac{\partial \delta_{ss}}{\partial \varphi} \tag{40}$$

$$\frac{\partial C}{\partial \delta} = \frac{D}{\delta - \delta_0} + \frac{\zeta D}{\delta - \delta_0}ln\left(\frac{\delta - \delta_0}{\delta_{ss}}\right) \tag{41}$$

$$\frac{\partial C}{\partial \varphi} = \frac{-D\delta_{ss}}{\delta - \delta_0}\left[\frac{1}{\delta_{ss}}\frac{\partial \delta_0}{\partial \varphi} + \frac{(\delta - \delta_0)}{\delta_{ss}^2}\frac{\partial \delta_{ss}}{\partial \varphi}\right] + ln\left(\frac{\delta - \delta_0}{\delta_{ss}}\right)D\left[\frac{\partial \zeta}{\partial \varphi}ln\left(\frac{\delta - \delta_0}{\delta_{ss}}\right) - \frac{\zeta\delta_{ss}}{\delta - \delta_0}\left(\frac{\partial \delta_0}{\partial \varphi}\frac{1}{\delta_{ss}} + \frac{(\delta - \delta_0)}{\delta_{ss}^2}\frac{\partial \delta_{ss}}{\partial \varphi}\right)\right] \tag{42}$$

$$\frac{\partial D}{\partial \delta} = \frac{\zeta}{\delta_{ss}}\left[\frac{\delta - \delta_0}{\delta_{ss}}\right]^{\zeta - 1} \tag{43}$$

$$\frac{\partial D}{\partial \varphi} = D\left[\frac{\partial \zeta}{\partial \varphi}ln\left(\frac{\delta - \delta_0}{\delta_{ss}}\right) - \frac{\zeta\delta_{ss}}{\delta - \delta_0}\left[\frac{1}{\delta_{ss}}\frac{\partial \delta_0}{\partial \varphi} + \frac{\delta - \delta_0}{\delta_{ss}^2}\frac{\partial \delta_{ss}}{\varphi}\right]\right] \tag{44}$$

References

[1] Needleman A. A continuum model for void nucleation by inclusion debonding. J Appl Mech Trans ASME 1987;54(3):525–31.
[2] Overgaard LC, Lund E. Structural collapse of a wind turbine blade. Part B: Progressive interlaminar failure models. Composites A 2010;41(2):271–83.
[3] Yang QD, Thouless MD. Mixed-mode fracture analyses of plastically-deforming adhesive joints. Int J Fract 2001;110(2):175–87.
[4] Hutchinson JW, Evans AG. Mechanics of materials: Top-down approaches to fracture. Acta Mater 2000;48:125–35.
[5] Hillerborg A, Modeer M, Petersson PE. Analysis of crack formation and crack growth in concrete by means of fracture mechanics and finite elements, Vol. 6. American Concrete Institute, ACI Special Publication; 1976, p. 773–82.
[6] Mohammed I, Liechti KM. Cohesive zone modeling of crack nucleation at bimaterial corners. J Mech Phys Solids 2000;48(4):735–64.
[7] Geubelle PH, Baylor JS. Impact-induced delamination of composites: a 2D simulation. Composites B 1998;29(5):589–602.

[8] Camacho GT, Ortiz M. Computational modelling of impact damage in brittle materials. Int J Solids Struct 1996;33(20–22):2899–938.
[9] Tvergaard V, Hutchinson JW. The influence of plasticity on mixed mode interface toughness. J Mech Phys Solids 1993;41(6):1119–35.
[10] Scheider I, Brocks W. Simulation of cup - cone fracture using the cohesive model. Eng Fract Mech 2003;70(14):1943–61.
[11] Xu XP, Needleman A. Void nucleation by inclusion debonding in a crystal matrix. Model Simul Mater Sci Fmg 1993;1:111–32.
[12] Ortiz M, Pandolfi A. Finite-deformation irreversible cohesive elements for three-dimensional crack-propagation analysis. Internat J Numer Methods Engrg 1999;44(9):1267–82.
[13] Li S, Thouless MD, Waas AM, Schroeder JA, Zavattieri PD. Mixed-mode cohesive-zone models for fracture of an adhesively bonded polymer-matrix composite. Eng Fract Mech 2006;73(1):64–78.
[14] Camanho P, Davila C. Mixed-mode decohesion finite elements in for the simulation composite of delamination materials. Nasa 2002;TM-2002-21(June):1–37.
[15] Camanho PP, Dávila CG, De Moura MF. Numerical simulation of mixed-mode progressive delamination in composite materials. J Compos Mater 2003;37(16):1415–38.
[16] Turon A, Camanho PP, Costa J, Dávila CG. A damage model for the simulation of delamination in advanced composites under variable-mode loading. Mech Mater 2006;38(11):1072–89.
[17] Sørensen BF, Gamstedt EK, Østergaard RC, Goutianos S. Micromechanical model of cross-over fibre bridging - prediction of mixed mode bridging laws. Mech Mater 2008;40(4–5):220–34.
[18] Sørensen BF, Goutianos S. Mixed mode cohesive law with interface dilatation. Mech Mater 2014;70:76–93.
[19] Park K, Paulino GH, Roesler JR. A unified potential-based cohesive model of mixed-mode fracture. J Mech Phys Solids 2009;57(6):891–908.
[20] Alfano G. On the influence of the shape of the interface law on the application of cohesive-zone models. Compos Sci Technol 2006;66(6):723–30.
[21] Gu P. Notch sensitivity of fiber-reinforced ceramics. Int J Fract 1993;70(3):253–66.
[22] Sørensen BF. Microscale testing and modelling for damage tolerant composite materials and structures. IOP Conf Ser: Mater Sci Eng 2020;942(1).
[23] Sørensen BF, Jørgensen K, Jacobsen TK, Østergaard RC. DCB-specimen loaded with uneven bending moments. Int J Fract 2006;141(1–2):163–76.
[24] Sørensen BF, Kirkegaard P. Determination of mixed mode cohesive laws. Eng Fract Mech 2006;73(17):2642–61.
[25] Sørensen BF, Jacobsen TK. Characterizing delamination of fibre composites by mixed mode cohesive laws. Compos Sci Technol 2009;69(3–4):445–56.
[26] Suo Z, Bao G, Fan B. Delamination R-curve phenomena due to damage. J Mech Phys Solids 1992;40(1):1–16.
[27] Rice JR. A path independent integral and the approximate analysis of strain concentration by notches and cracks. J Appl Mech 1968;35(2):379–88.
[28] Needleman A. Micromechanical modelling of interfacial decohesion. Ultramicroscopy 1992;40:203–14.
[29] Stigh U, Svensson D. On cohesive laws for delamination of composites. In: European conference on composite materials, Vol. 14. 2010, p. 1–10.
[30] Goutianos S, Drews J. Estimation of interface cohesive laws by digital image correlation. In: 28th Risø symposium on interface design of polymer matrix composites. 2007, p. 181–90.
[31] De Souza JA, Goutianos S, Skovgaard M, Sørensen BF. Fracture resistance curves and toughening mechanisms in polymer based dental composites. J Mech Behav Biomed Mater 2011;4(4):558–71.
[32] Erives R, Goutianos S, Sørensen BF. Characterising mix-mode delamination of unidirectional composites under large-scale bridging. 2022.
[33] Thouless MD. 2020. Private communication.
[34] Goutianos S, Sørensen BF. Path dependence of truss-like mixed mode cohesive laws. Eng Fract Mech 2012;91:117–32.
[35] van den Bosch MJ, Schreurs PJ, Geers MG. An improved description of the exponential xu and needleman cohesive zone law for mixed-mode decohesion. Eng Fract Mech 2006;73(9):1220–34.
[36] Goutianos S, Sørensen BF. Fracture mechanics analysis of composites with ply-drops - measurement of delamination fatigue crack growth rate. In: ECCM 2018 - 18th European conference on composite materials. 2020.
[37] Joki RK, Grytten F, Hayman B, Sørensen BF. Determination of a cohesive law for delamination modelling - accounting for variation in crack opening and stress state across the test specimen width. Compos Sci Technol 2016;128:49–57.